sustainability

MDPI

Article

Optical Properties and Gamma Radiation Shielding Capability of Transparent Barium Borosilicate Glass Composite

Mohamed Ehab [1,*], Elsayed Salama [2,*], Ahmed Ashour [1], Mohamed Attallah [3] and Hosam M. Saleh [4]

[1] Engineering Mathematics and Physics Department, Faculty of Engineering and Technology, Future University in Egypt (FUE), New Cairo 11845, Egypt
[2] Basic Science Department, Faculty of Engineering, The British University in Egypt (BUE), El Sherouk City 11837, Egypt
[3] Basic Science Department, Higher Technological Institute, 10th of Ramadan City 44629, Egypt
[4] Radioisotope Department, Nuclear Research Center, Egyptian Atomic Energy Authority, Cairo 11787, Egypt
* Correspondence: mehab@fue.edu.eg (M.E.); elsayed.salama@bue.edu.eg (E.S.); Tel.: +20-1223870849 (E.S.); Fax: +20-2-24665630 (E.S.)

Abstract: In this study, both radiation shielding capability and optical properties of prepared SiO_2-ZnO-Na_2CO_3-H_3BO_3-$BaCO_3$ glass composite with different concentrations of barium carbonate (0–30 mol%) have been studied. Gamma attenuation properties, such as the mass attenuation coefficient (MAC), mean free path (MFP), and exposure build-up factor (EBF), are experimentally and theoretically investigated. The detected XRD patterns for the prepared glass composites confirm their amorphous nature. It is evident from the obtained data that all tested parameters, such as mass density, molar volume, refractive index, dielectric constant, refraction loss (%), and molar refraction, have been increased as $BaCO_3$ mol% increased. At the same time, the results of the optical bandgap show a gradual decrease with increasing barium concentration. It was also found that the mass attenuation coefficients increased with $BaCO_3$ concentration from 0.078 at zero mol% $BaCO_3$ to 0.083 cm^2/g at 30 mol%. Moreover, the half-value layer (HVL) and the exposure build-up factor (EBF) up to 40 mfp penetration depth were investigated in addition to the effective atomic number (Z_{eff}) and the corresponding equivalent atomic number (Z_{eq}) at the energy range of 0.015–15 MeV. The produced glass composite might be considered for many shielding applications based on the obtained results that require a transparent shielding material.

Keywords: mass attenuation coefficient; effective atomic number; build-up factor; borosilicate glass; radiation shielding

Citation: Ehab, M.; Salama, E.; Ashour, A.; Attallah, M.; Saleh, H.M. Optical Properties and Gamma Radiation Shielding Capability of Transparent Barium Borosilicate Glass Composite. *Sustainability* **2022**, *14*, 13298. https://doi.org/10.3390/su142013298

Academic Editor: Changhyun Roh

Received: 7 July 2022
Accepted: 9 October 2022
Published: 16 October 2022

1. Introduction

Shielding materials have a significant role in radiation protection during the wide medical use of radioactive isotopes and X-ray machines and in many industrial applications, such as petroleum and gas extraction [1]. The shielding of ionizing radiation has significantly changed over the last 60 years. As a result of these ongoing developments in anti-ionizing radiation technology, the significance of composite materials for radiation shielding has been acknowledged. In shielding applications, composite materials are desirable because secondary radiation must be considered in radiation shielding design. Therefore, a functional shield's composition must be such that it can efficiently absorb both primary and secondary radiation rays. In addition to their ability to absorb all primary and likely secondary radiation, other properties might restrict the use of particular materials for radiation shielding, such as space, cost, mechanical strength, chemical stability, and thermal stability.

There is a continuing need for new materials to be employed as shielding materials under testing nuclear radiation exposure circumstances [2–5]. The most often utilized protective material so far is concrete [5–10], which is cement mixed with various additives,

such as cellulosic waste [11,12], bitumen [13,14], glass [15], polymers [16–18], nanomaterials [19,20], and cement wastes [21,22]. However, the trouble in accomplishing homogeneity, the presence of water and the need for transparency of the shield have persuaded scientists to use glass rather than concrete [23–27]. Borate glasses are used for their exceptionally high transparency, low melting point, and thermal stability. The role of glass additives is different depending on the kind of the enhancement property. Adding sodium carbonate (Na_2CO_3) to the borate glass improves its glass nature characterizations by changing the coordination of the boron coordination group [19], while zinc oxide (ZnO) is added to borate glass to boost its thermal stability, reduce crystallization, and enhance the glass matrix's chemical resistance [28–32]. Heavy elements, such as lead, barium, bismuth, and tungsten are used to increase the borate glass density, which in turn greatly enhancing their radiation-shielding abilities [5,27,33,34]. Borated glasses doped with lead and other specific elements to enhance their densities and radiation attenuation characteristics are successfully produced [32,35–37]. Borosilicate glasses have further advantages, such as chemical durability, better heat stability, extremely low thermal expansion coefficients, and high capacities for substantial visible light transmission [38–41].

Due to its high atomic number and good attenuation coefficient, barium-based glasses have a very promising gamma radiation attenuation coefficient. Several borosilicate glass systems were tested as gamma-ray shielding materials doped with different metal oxides, such as PbO, BaO, Bi_2O_3, BaO, TiO_2, and SrO at different concentrations, showed better shielding efficiencies compared with those previously used in the industry [26,27,42–46]. Adding iron (III) oxide to sodium-barium-vanadate glass has an impact on its physical, optical, mechanical, and radiation absorption features where significant effect on the interaction parameters of thermal neutrons and gamma radiation absorption are observed [47]. The prepared titanium borosilicate glass modified with various ratios of barium oxide showed that adding barium increased the attenuation parameters and enhanced the durability of the prepared sample [48]. The density of sodium zinc borate glasses doped with dysprosium and barium oxide was observed to increase from 2.30 to 4.02 g/cm^3, and the glass's hygroscopic property considerably decreased with the addition of barium [49]. The addition of BaO to zinc barium tellurite glasses enhances its polarization by increasing the bond length, hence the glass network expansion resulting in volume.

The current work aims to prepare and investigate highly transparent, lead-free barium borosilicate glass composite to be used for gamma shielding applications.

2. Materials and Methods

The glass composite of 10 Na_2CO_3 − 20 SiO_2 − 10 ZnO − (60 − x) H_3BO_3 − x $BaCO_3$ (where x = 0, 5, 10, 20, and 30 mol%) was fabricated using the conventional fast melt-quenching technique. High purity grade powders of Na_2CO_3, SiO_2, ZnO, H_3BO_3, and $BaCO_3$ were utilized as a starting material, as shown in Table 1. The compositions were mashed in an agate mortar and melted at 1100 °C for one hour in a porcelain crucible and twirled a lot until a homogenous bubble-free liquid was formed. The melts were poured into preheated stainless-steel molds and annealed at ∼400 °C for 4 h to reduce the cracking and thermal stresses of the samples and then left to cool to room temperature. The photos of the obtained samples before polishing are shown in Figure 1. The samples were then manually polished to obtain maximum flatness.

Table 1. Samples compositions (mol%).

Sample	Na_2CO_3	SiO_2	ZnO	H_3BO_3	$BaCO_3$
S0	10	20	10	60	0
S1	10	20	10	55	5
S2	10	20	10	50	10
S3	10	20	10	40	20
S4	10	20	10	30	30

Figure 1. Photos of the prepared samples.

X-ray diffraction (XRD) was accomplished for the prepared glass powders by utilizing a Philips X'pert Pro X-ray powder diffractometer (Malvern Panalytical, Almelo, The Netherlands) at room temperature. The X-ray diffraction patterns were analyzed in 2θ scan from 10° to 90° with CuKα as a target and Ni as a filter (λ = 1.5418 Å) at 40 KV and 30 mA with a speed of scanning reaching to 0.3 s.

Fourier transformation of the infrared absorption spectra (FTIR) of the produced samples were measured in the spectral region 400–4000 cm^{-1} using a JASCOFT-IR6200 spectrometer with the KBr pellet method.

The densities of the prepared glass specimens were measured at room temperature by a simple Archimedes technique that utilizes xylene as a submerged liquid according to the following formula [50]:

$$\rho = \frac{W_a}{W_a - W_b}\rho_b \quad (1)$$

where W_a is the sample's weight in air, W_b represents its weight in xylene, and ρ_b is xylene's density ($\rho_b = 0.863\ g/cm^3$). Using the results of the mass density, the molar volume of the glasses can be calculated according to the following formula [51]:

$$V_m = M_W/\rho \quad (2)$$

where M_W is the molecular weight, and ρ is the glass sample density. Subsequently, the refractive index of the prepared samples can be calculated by the following relation [39,51]:

$$n = \left(\frac{\rho + 10.4}{8.6}\right) \quad (3)$$

Other features depending on the refractive index can be acquired, such as the dielectric constant, which can be calculated according to the following formula [52]:

$$\varepsilon = n^2 \quad (4)$$

Additionally, the reflection loss (R) has been calculated by using the following Fresnel's formula [53]:

$$R = \left(\frac{n-1}{n+1}\right)^2 \quad (5)$$

The ratio of molar volume to molar refractivity (R_M), which is acquired and calculated via the following equation [52], is another structural correlation that can be used to forecast glass propensity that would be metallic or insulating.

$$R_M = V_m\left(\frac{n^2-1}{n^2+2}\right) \quad (6)$$

A recording double beam UV-VIS spectrophotometer (type JASCO Crop., V-770, Japan) encompassing the wavelength range from 200 to 1100 nm was used to evaluate the optical absorption spectra of the polished samples. The absorption coefficient and optical bandgap

of the samples were determined according to the optical absorption data. The optical absorption coefficient α (ν) was calculated utilizing the following equation [52]:

$$\alpha(\nu) = 2.303A/d \tag{7}$$

where A is the absorbance, and d is the thickness of the glass sample. Then, the optical bandgap (E_{opt}) is determined through the well-known relation [54]:

$$\alpha(\nu) = B\,\frac{(h\nu - E_{opt})^n}{h\nu} \tag{8}$$

where hν is the incident photon energy, and B is a constant relating to the band tailing's extent.

For direct allowed, indirect allowed, direct forbidden, and indirect forbidden transitions, respectively, the index n has the values 1/2, 2, 3/2, and 3. Since there is no transition symmetry in the case of indirect transitions, the electron's wave vector might change during the optical transition, and phonons will either take or give up the momentum shift. [55]. In the above-mentioned case, $(\alpha h\nu)^{0.5}$ renders a linear relation with the photon energy. Extrapolating of the linear part of the overhead relation shows the optical bandgap E_{opt} where $(\alpha h\nu)^{0.5} = 0$ in case of indirect transition.

A NaI (Tl) scintillation detector (Teledyne Isotopes "2 × 2" NaI (Tl) Scintillation Detector, AL, USA) with an energy resolution of 8% at 662 keV was used to test the gamma-ray shielding properties of the set glass samples. The generated glass samples were measured at four distinct gamma energies under the correct geometrical constraints: 0.662 MeV from a Cs-137-point source, 0.239 MeV, 0.911 MeV from a 232 Th point source, and 1.332 MeV from a Co-60-point source. All these sources are provided by a spectrum techniques company. The investigated samples were polished and formed to have cylindrical shape of about 2 cm diameter and 1 cm thickness. During the measurements of the gamma attenuation coefficients, the sample was in contact with the point source, and the distance between the source and the detector was fixed at about 10 cm.

3. Theoretical Background

Modified Lambert-Beer law was utilized for the calculation of the linear attenuation coefficients as follows [23]:

$$I = I_0 \times B \times e^{-\mu x} \tag{9}$$

where I_0 and I are the initial and transmitted photon intensities, respectively, μ is a linear attenuation coefficient (cm^{-1}), and B (E, x) is the build-up factor depending on the thickness x (cm) of the used material and the energy E of the incident photon. The mass attenuation coefficient (μ_m) can be determined utilizing the measured linear attenuation coefficient and the mass density (ρ) values by the following relationship [36]:

$$\mu_m = \frac{\mu}{\rho} \tag{10}$$

The following formula can be used to determine μ_m for a compound or mixture [54]:

$$\mu_m = \sum_i w_i(\mu_m)_i \tag{11}$$

where $(\mu_m)_i$ is the mass attenuation coefficient of the examined mixture's ith element and w_i stands for its weight percentage. The half-value layer (HVL) of the prepared glasses can be calculated by the following formula [53,56]:

$$HVL = \frac{0.693}{\mu} \tag{12}$$

where μ is the material's linear attenuation coefficient, which obviously relies on the material's type, mass density, and beam energy.

The National Institute of Standard and Technology (NIST) created a photon cross-sections database called XCOM that contains the attenuation coefficients of all elements in the periodic table at various energies in order to calculate the values of the mass attenuation coefficients for the glass samples over a broad range of energies from 0.015 to 15 MeV [57]. The following equation was used to compute the mean free path (MFP) values using the linear attenuation coefficient [58]:

$$\mathrm{MFP} = \frac{1}{\mu} \tag{13}$$

The effective atomic number of a material (Z_{eff}) is defined as the ratio of an object's electronic cross-section (σ_a) to its effective atomic cross-section (σ_e). For the produced glass samples, the following relationship may be used to estimate the values of Z_{eff} based on the obtained data of μ_m [33]:

$$Z_{eff} = \frac{\sigma_a}{\sigma_e} = \frac{\sum_i f_i A_i (\mu_m)_i}{\sum_i f_i \frac{A_i}{Z_i} (\mu_m)_i} \tag{14}$$

where A_i is the atomic weight, Z_i is the atomic number, $(\mu_m)_i$ is the mass attenuation coefficient for the ith element, and f_i represents ith element fractional abundance concerning the number of atoms. To calculate the build-up factor, we must first obtain the Compton partial attenuation coefficient ($(\mu_m)_{comp}$) and total attenuation coefficient ($(\mu_m)_{total}$) values for the constituent elements and compounds of the examined glass samples in the energy range of 0.015–15.0 MeV. The values of the equivalent atomic number (Z_{eq}) for the produced glass samples may then be computed by comparing the ratio $(\mu_m)_{comp}/(\mu_m)_{total}$ at a certain energy with comparable ratios of elements at the same energy. The interpolation of the equivalent atomic number was determined using the following logarithmic interpolation algorithm [59] where the ratio $(\mu_m)_{comp}/(\mu_m)_{total}$ lies between two subsequent ratios of elements:

$$Z_{eq} = \frac{Z_1(\log R_2 - \log R) + Z_2(\log R - \log R_1)}{\log R_2 - \log R_1} \tag{15}$$

where the atomic numbers of the pure elements corresponding to the ratios R_1 and R_2 are Z_1 and Z_2, respectively, and R is the ratio for studied glass samples at certain energy [60]. Using the general progressive (G-P) interpolation in the energy range of 0.015–15 MeV up to 40 mfp, the exposure build-up factors EBF were calculated for the prepared above-mentioned glass samples utilizing the following equations as mentioned in Harima et al. (1993) [6,61,62]:

$$B(E, X) = 1 + \frac{b-1}{K-1}(K^x - 1) \text{ for } K \neq 1 \tag{16}$$

$$B(E, X) = 1 + (b-1)X \text{ for } K = 1 \tag{17}$$

$$K(E, X) = cX^a + d\frac{\tanh\left(\frac{X}{X_K} - 2\right) - \tan h(-2)}{1 - \tan h(-2)} \tag{18}$$

where E is the photon energy, X is the separation between the detector and the source as a function of MFP, B is the EBF value at 1 MFP, K (E, X) is the dosage multiplicative factor, and b, c, a, X_K and d are the calculated G-P fitting parameters that rely on the attenuating medium and source energy. The prepared glasses' b, c, a, X_K and d G-P fitting parameters can be interpolated logarithmically using the following equation-like method for the 0.015–15 MeV gamma-ray energy range up to 40 mfp [63,64].

$$P = \frac{P_1\left(\mathrm{loglog}\, Z_2 - \mathrm{loglog}\, Z_{eq}\right) + P_2\left(\mathrm{loglog}\, Z_{eq} - \mathrm{loglog}\, Z_1\right)}{\mathrm{loglog}\, Z_2 - \mathrm{loglog}\, Z_1} \tag{19}$$

P_1 and P_2 are the values of the G-P fitting parameters that correspond to the Z_1 and Z_2 atomic numbers at the specified energy, respectively. The American Nuclear Society's study criteria for G-P fit for the elements were used [65].

4. Results and Discussion

4.1. XRD Analysis and FTIR

The XRD patterns for the prepared glass samples were obtained and are shown in Figure 2. The absence of sharp peaks in the XRD results demonstrates that the prepared specimens have an amorphous nature. The two humps seen at 2θ° equal 25° and 45° for each sample and serve as a strong piece of evidence for the constructive interferences at variance of two and the aggregation of atoms in the glass matrix in two separate ways. A typical peak for borosilicate matrices was previously seen in several publications [45,66,67].

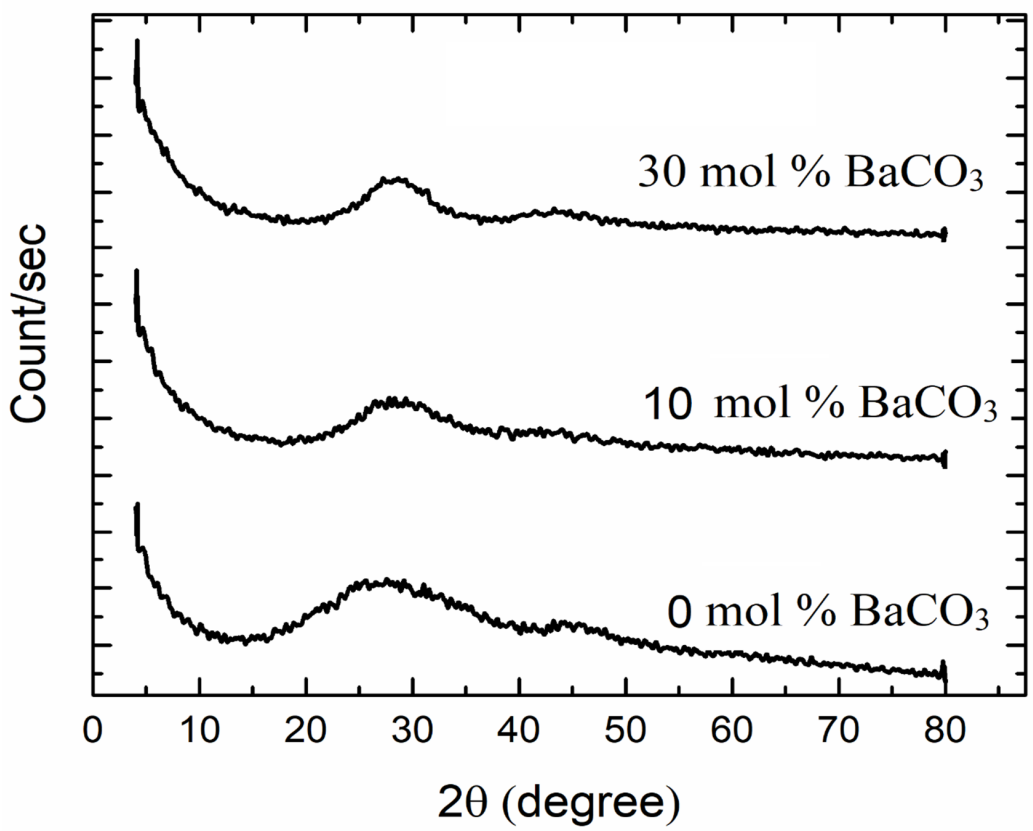

Figure 2. Patterns of X-ray diffraction for ZnO borosilicate glasses doped with $BaCO_3$.

The FTIR transmission spectra of ZnO borosilicate glasses doped with different concentrations of $BaCO_3$ are shown in Figure 3. Table 2 displays the results of the FTIR absorption bands and the associated vibrational modes.

Four distinct bands can be found in the observed data. The band located between 800 and 1200 cm^{-1} represented the BO_4 structural units. Two more bands were visible in the range of 600 and 800 cm^{-1} and 1200 to 1600 cm^{-1} and were returned to BO_3 structural units. Finally, the band of metal ion vibrations was observed at 400 to 600 cm^{-1}. The stretching relaxation modes of B–O bonds of trigonal BO_3 band centered at 1364 cm^{-1} is observed with a small shoulder edge around 1260 cm^{-1} [68]. While the strong broad band from 1176–755 cm^{-1} centered at 955 cm^{-1} are attributed to asymmetric stretching of B–O bonds of tetrahedral BO_4 units. The higher intensity observed may be due to the formation of Si–O–Si and B–O–Si bonds, which contribute vibrational modes at the BO_4 band [70–72]. A moderate band centered around 700 cm^{-1} may be due to bending vibrations of B–O–B of linkages in a borate network [73,74]. The band centered at 440 cm^{-1} and the shoulder noticed at 500 cm^{-1} may be attributed to vibrational modes of all metal cations Ba^{+2} and Zn^{+2} [75–77]. It is noticed that the increase in the $BaCO_3$ mol% in the composite shifts the bands to a lower wavenumber, which denotes a reduction in the BO_3 group and formation

of the BO_4 in the glass structure. As a result, an increase in non-bridging oxygens (NBO) and a decrease in the degree of localization of electrons are produced.

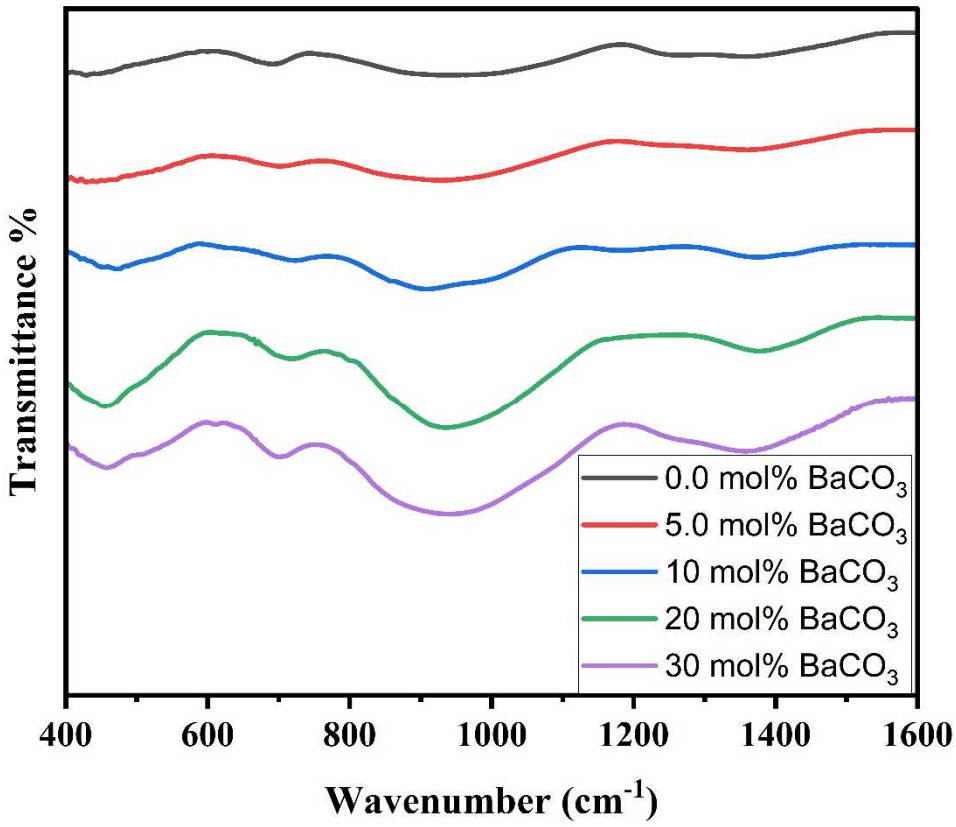

Figure 3. FTIR for ZnO borosilicate glasses doped with $BaCO_3$.

Table 2. The assigned infrared bands to the produced glass samples' spectra.

Peak Position (cm^{-1})	Assignment	Reference Range
1364	Stretching relaxation of B–O bonds of trigonal BO_3 units	1170−1600 [68,69]
950	Stretching vibrations of B–O–Si linkages	950−1050 [70,71]
926	Stretching vibrations of B–O bonds of tetrahedral BO_4 units.	800–1200 [43,71,72]
705	B–O–B vibrations of linkages in a borate network	~700 [73,74]
451	Vibrations of the metal cations Ba^{+2} and Zn^{+2}	400−600 [75,77]

4.2. Density and Molar Volume

Figure 4 displays the mass densities and molar volumes of the produced glasses. Both the density and the molar volume show an equivalent trend increase with increasing the $BaCO_3$ mol% in the composites. By increasing the $BaCO_3$ mol% in the composite, the structure becomes more compact. The larger molecular weight of BaCO3 relative to the other elements may have contributed to the rise in density. On the contrary, the increases in molar volume may be related to the creation of non-bridging oxygen ions (NBOs), which tend to increase the randomizer in the network and convert triangular (BO_3) structure units into tetrahedral (BO_4) structure units [46,78].

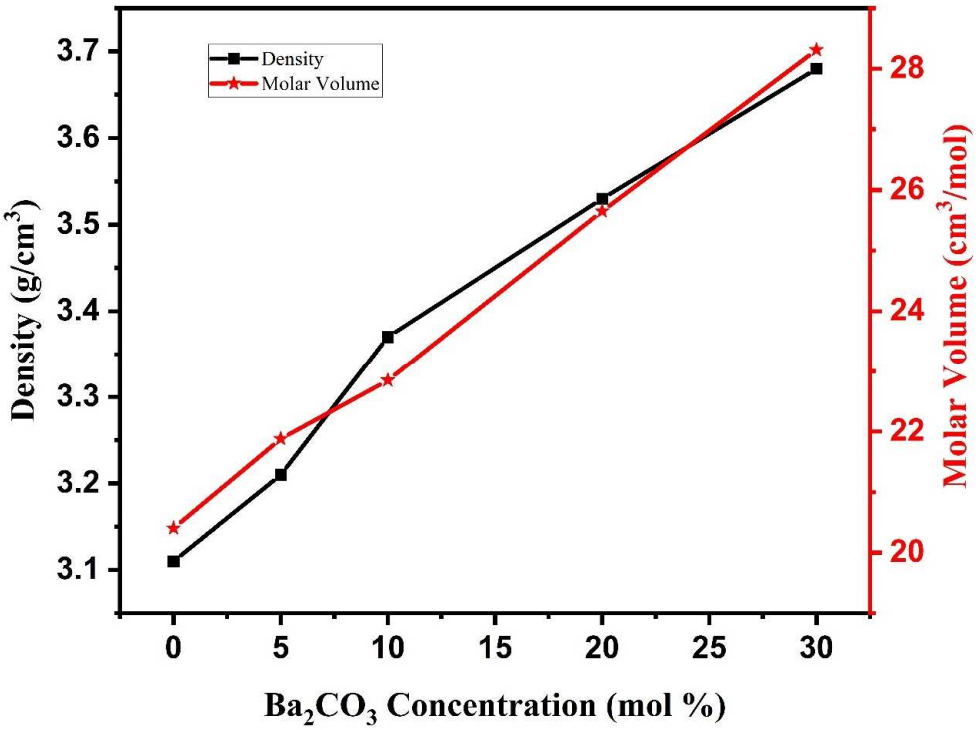

Figure 4. Density and molar volume for ZnO borosilicate glasses doped with $BaCO_3$.

4.3. Optical Absorption Spectra

A powerful technique used to express the optical transitions and electronic band configuration of the amorphous materials is the absorption edge in the region of UV-Vis. Therefore, the optical absorption spectra for set glass samples are shown in Figure 5. The consistency of each sample has been kept as small as possible to evade the inherent absorbance resulted from the long optical path length.

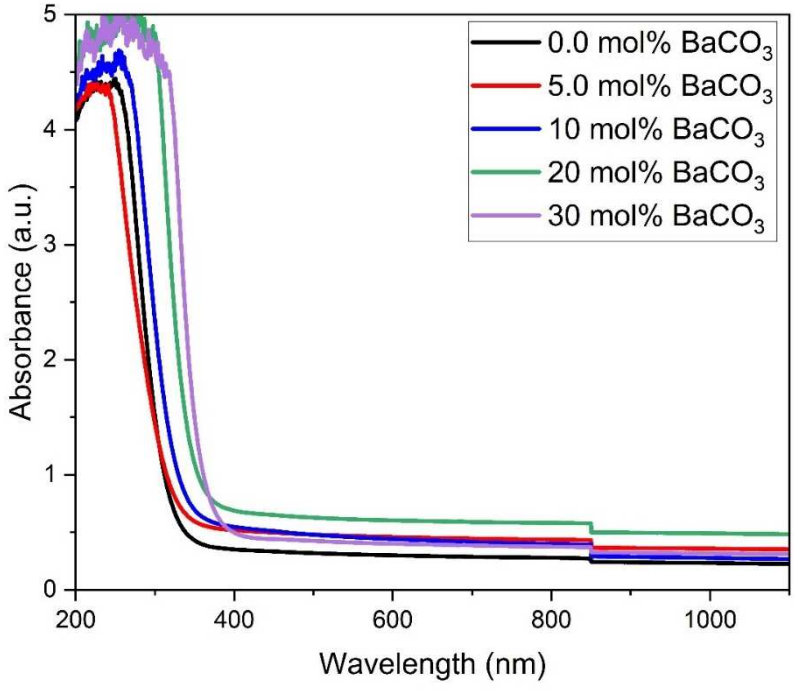

Figure 5. Absorbance versus wavelength for ZnO borosilicate glasses as a function of $BaCO_3$ mol%.

The linear relation between $(\alpha h\nu)^{0.5}$ and the photon energy is shown in Figure 6. Extrapolating of the linear part of the overhead relation shows the optical bandgap E_{opt} energies of 3.55, 3.42, 3.29, 3.21, and 3.13 eV. The values of optical bandgap performance show a gradual decrease with increasing barium concentration. The observed decrease in bandgap with improved $BaCO_3$ mole% concentration could be attributable to potential flaws in the glass network as non-bridging oxygen (NBO) ranges rise. It also indicates the formation of new localized states formed between the valence and conductive bands. Finally, because of the usage of $BaCO_3$ rather than boron oxide, the glass matrix is densified, which is well compatible with the resulting density and changes in the optical bandgap.

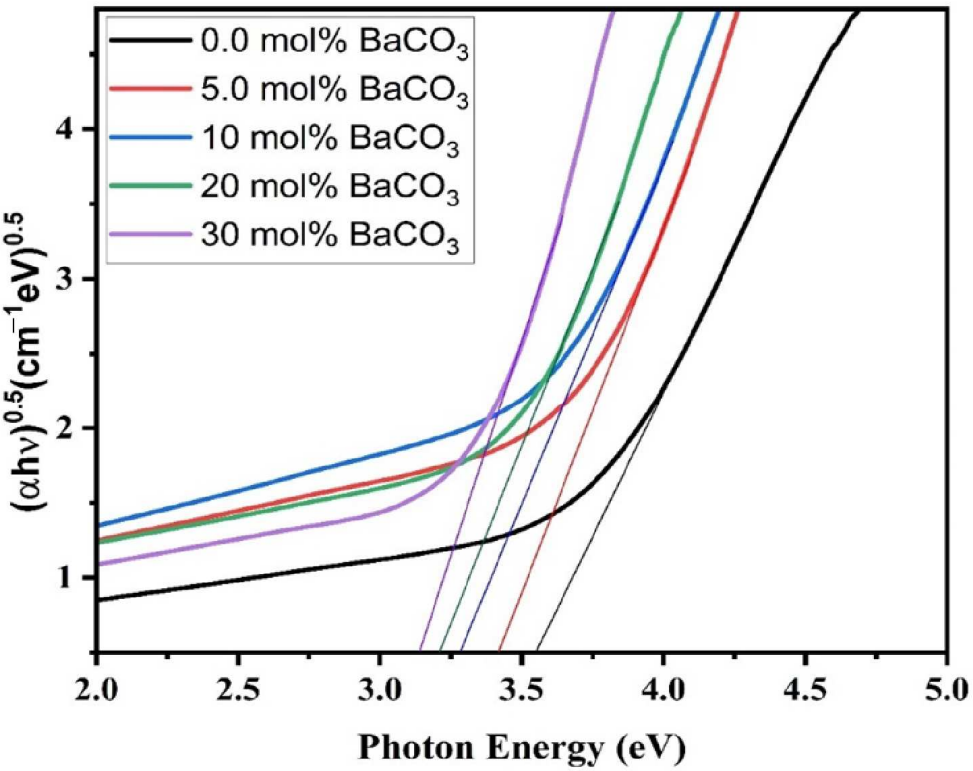

Figure 6. Optical bandgap for ZnO borosilicate glasses as a function of $BaCO_3$ mol%.

The received data of the refractive index and its related parameters are summarized in Table 3. It is evident from the obtained data that all these parameters have the same trend. With increasing $BaCO_3$ mol%, the parameters grew linearly. All estimated parameters confirm the role of barium oxide in the glass network. It has been observed that the refractive index increases as the $BaCO_3$ mol% increases inside the structure grow. The compactness that rises in the glass samples can be linked to this boom in the refractive index.

4.4. Mass Attenuation Coefficient

Table 4 compares the values of the mass attenuation coefficient (μ_m) that were derived theoretically and experimentally. It has been established that there is a close correlation between experimental and theoretical values. Figure 7 displays the fluctuation of m for the produced glass samples with photon energies ranging from 0.015 to 15 MeV. The obtained values of μ_m significantly boost the growth in $BaCO_3$ concentration at the same photon energy while mimicking the chemical composition and photon energy. Based on the interaction of gamma radiation with the examined material, it is possible to explain the inverse relationship between m and the rise in energy for all samples. The photoelectric effect is the most common interaction at low photon energies (E), with an interaction probability proportional to $E^{-3.5}$. While Compton scattering is the dominant interaction at

intermediate energies, its probability of interaction is proportional to E^{-1}. Pair production is most prevalent at very high photon energies over 1.022 MeV, where the chance of contact is proportional to E^2. The little variation in the mass density of the prepared glass samples with an increase in BaCO3 concentration from 0 to 30 mol% is what causes the Compton mass attenuation fraction to remain constant. As a result, the mass attenuation coefficient of the produced glass samples has been significantly increased in low-energy areas where x-ray shielding applications are advantageous. The K-absorption edge of barium is what causes the observed peak at around 0.04 MeV (0.037 MeV).

Table 3. Physical parameters of the prepared glass system.

Physical Parameter	$BaCO_3$ mol%				
	0	5	10	20	30
Density (g/cm^3)	3.11	3.21	3.37	3.53	3.68
Molar volume (cm^3 mol^{-1})	33.69	33.77	33.91	33.96	34.52
Refractive index	1.57	1.58	1.59	1.61	1.63
Dielectric constant	2.46	2.5	2.54	2.62	2.68
Refraction loss (%)	0.049	0.050	0.052	0.055	0.058
Molar refraction (cm^3)	11.07	11.29	11.51	11.91	12.39
The optical bandgap (eV)	3.55	3.42	3.29	3.21	3.13

Table 4. The mass attenuation coefficients (cm^2/g) of the created glass samples, both theoretically and experimentally.

$BaCO_3$ (mol%)	0.662 MeV			1.173 MeV			1.332 MeV		
	Exp.	Theo.	% Diff,	Exp.	Theo.	% Diff	Exp.	Theo.	% Diff
0	0.078 ± 0.006	0.078	0.0	0.056 ± 0.006	0.059	5.4	0.055 ± 0.003	0.056	1.8
5	0.078 ± 0.006	0.078	0.0	0.059 ± 0.004	0.059	0.0	0.054 ± 0.002	0.055	1.9
10	0.078 ± 0.006	0.078	0.0	0.049 ± 0.004	0.058	17	0.056 ± 0.003	0.054	3.6
20	0.079 ± 0.006	0.078	1.3	0.054 ± 0.004	0.057	5.6	0.054 ± 0.002	0.053	1.9
30	0.083 ± 0.005	0.078	6.0	0.051 ± 0.004	0.056	7.8	0.054 ± 0.002	0.053	1.9

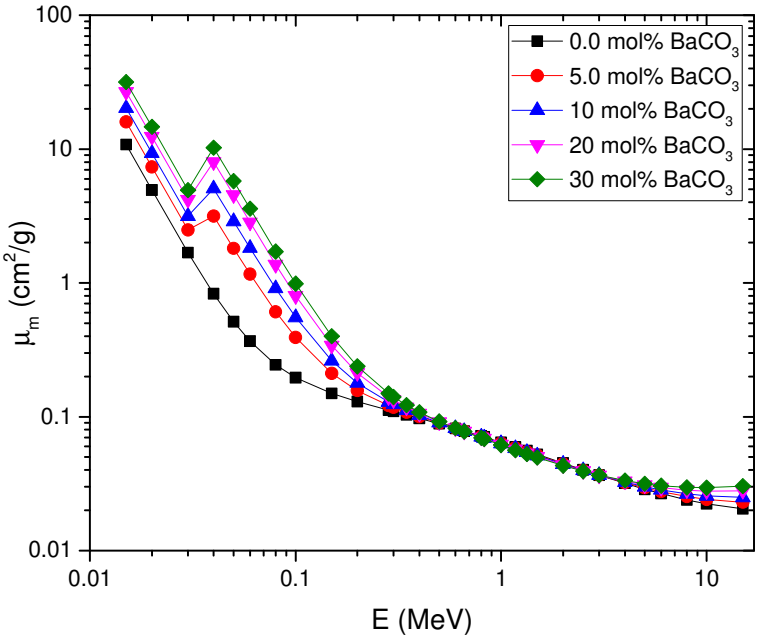

Figure 7. Mass attenuation coefficients of 10 Na_2CO_3 − 20 SiO_2 − 10 ZnO−(60 − x) H_3BO_3 − x $BaCO_3$ glass system in the energy ranges from 0.015–15 MeV and x = 0, 5, 10, 20, 30.

4.5. Half Value Layer (VL) and Effective Atomic Number (Z_{eff})

Figure 8 depicts the fluctuation in the produced glass composite's effective atomic number (Zeff) at energies between 0.015 and 15 MeV and at various concentrations of $BaCO_3$. The observed increase in the Z_{eff} with the increase in the barium concentration can be attributed to the higher atomic number for barium compared with boron (barium is added on the expense of boron) while the change in Z_{eff} of the prepared glass composite in the investigated energy range 0.015–15 MeV can be explained based on the probability of gamma radiation interaction at each energy photon. At low energy range, photoelectric reaction dominates, with the probability proportional to Z^4. As the incident photon energy increases, photo electric interaction probability will decrease, and therefore, Z_{eff} will also decrease. At the intermediate energy range, Compton interaction dominates, with the probability proportional to Z. As the incident photon energy increases, Compton interaction probability will decrease (Compton interaction probability proportional with E^{-1}), and therefore, Z_{eff} will also decrease. At the higher energy range, more than 1.022 MeV pair production interaction dominates, with the probability proportional to Z^2. As the incident photon energy increases, pair production interaction probability will increase, and therefore, Z_{eff} will also increase [79]. At about 0.04 MeV, the ultimate Z_{eff} value was detected in all the prepared glass samples. As discussed in the attenuation curve, maximum absorption occurred at the K-absorption edge of barium at about 0.037 MeV.

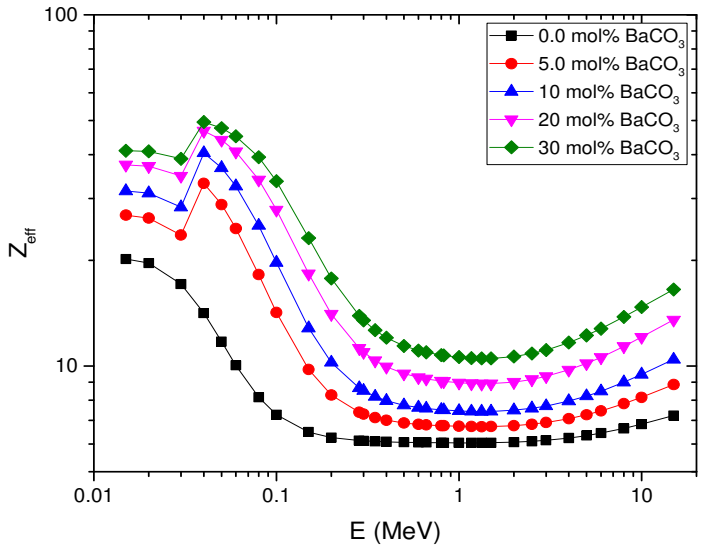

Figure 8. Z_{eff} results of 10 Na_2CO_3 − 20 SiO_2 − 10 ZnO − (60 − x) H_3BO_3 − x $BaCO_3$ glass system.

The results of the calculated values of the half value layer (HVL) at the same energy range 0.015–15 MeV are shown in Figure 9. The discussion of these results is the same as mentioned in the case of the mass attenuation coefficients.

4.6. The Exposure Build-Up Factor (EBF)

As shown in Figure 10, the exposure build-up factor (EBF) values for the prepared glass samples (S0–S4) were calculated using the geometrical progression (G-P) method with depth penetration of up to 40 mfp and photon energies of up to 15 MeV. The picture also demonstrates that, according to the photoelectric effect interaction mechanism, the EBF values of the produced glass samples are negligible at low photon energies. Additionally, within the intermediate energy range when numerous scatterings about the Compton interactions has happened, the samples' EBF significances rise with the energy of the photons. The calculated EBF values for the pair formation process increase at high photon energies. Additionally, strong peaks can be seen at 0.04 MeV in Figure 8 due to the K-absorption edge of barium (0.037 MeV).

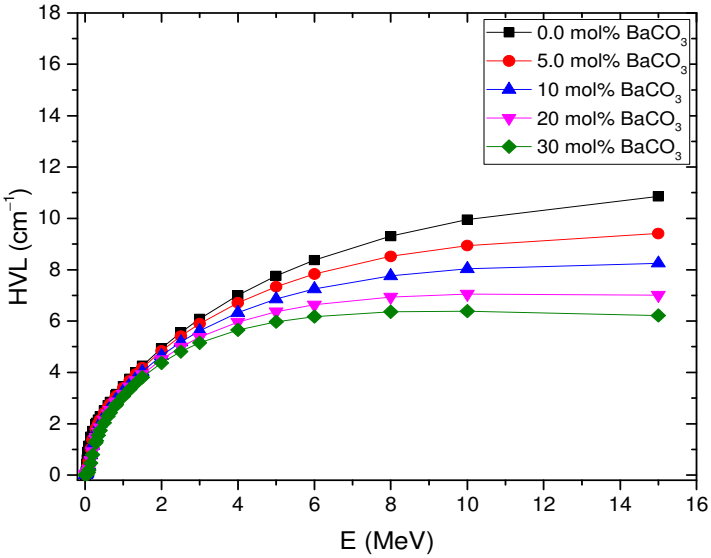

Figure 9. HVL results of 10 Na_2CO_3 − 20 SiO_2 − 10 ZnO − (60 − x) H_3BO_3 − x $BaCO_3$ glass system.

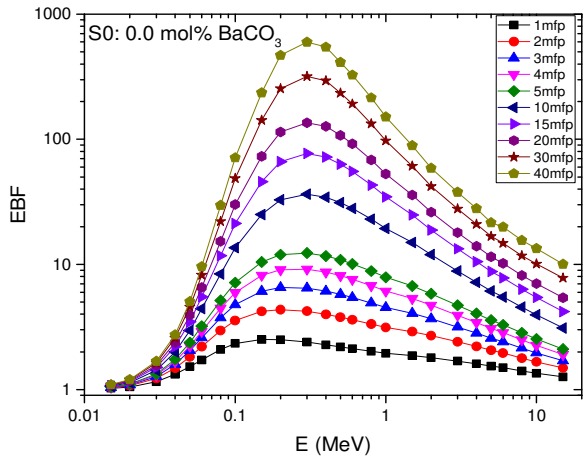

(**a**)

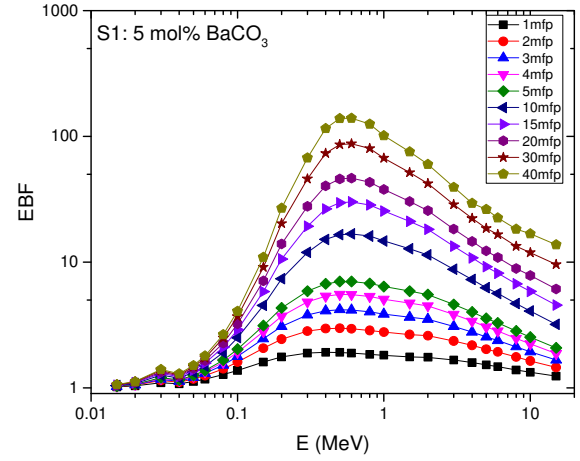

(**b**)

Figure 10. *Cont.*

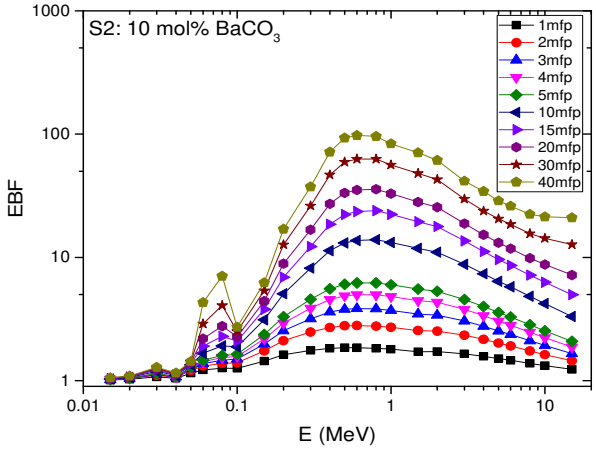

(**c**)

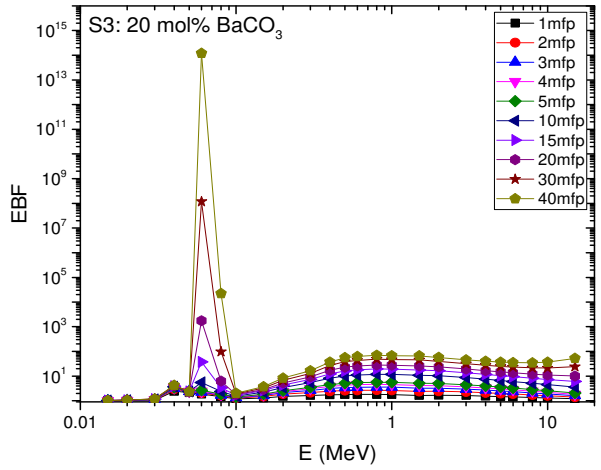

(**d**)

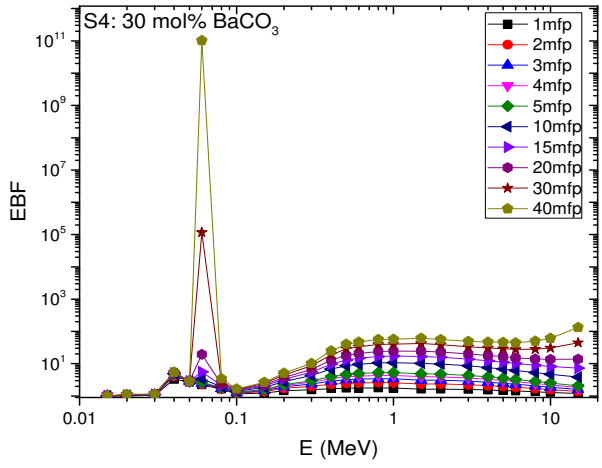

(**e**)

Figure 10. EBF of the produced borosilicate glass composite at 0.015 to 15 MeV up to 40 mfp photon energies with (**a**) 0 mol% $BaCO_3$, (**b**) 5 mol% $BaCO_3$, (**c**) 10 mol% $BaCO_3$, (**d**) 20 mol% $BaCO_3$, and (**e**) 30 mol% $BaCO_3$.

5. Conclusions

The glass composites 10 Na_2CO_3 − 20 SiO_2 − 10 ZnO − (60 − x) H_3BO_3 − x $BaCO_3$ in the current study have been made using the traditional melting procedure, where x = 0, 5, 10, 20, 30. The parameters for structural, optical, and gamma attenuation are established. With the addition of $BaCO_3$, the molar volume and mass density measurements revealed an improvement in compactness. Different vibrational bonding modes, including B–O, B–O–B, and B–O–Si, were seen in the produced glasses according to the FTIR data. The effective atomic number (Z_{eff}), mass attenuation coefficients (MAC), and exposure build-up factors (EBF) of the previously described prepared glass samples were computed at various photon energies between 0.015 and 15 MeV. The findings attained may recommend the manufactured glasses for applications requiring transparent shielding.

Author Contributions: Formal analysis, E.S.; Methodology, M.E., E.S., A.A. and M.A.; Supervision, E.S. and H.M.S.; Writing—original draft, M.E. and M.A.; Writing—review & editing, E.S. All authors have read and agreed to the published version of the manuscript.

Funding: This research received no external funding.

Institutional Review Board Statement: Not applicable.

Informed Consent Statement: Not applicable.

Data Availability Statement: Not applicable.

Conflicts of Interest: The authors declare no conflict of interest.

References

1. Majeed, K.F.; Salama, E.; Elfiki, S.A.; Al-Bakhat, Y.M.Z. Natural radioactivity assessment around the petroleum-producing areas of The-Qar province, Iraq. *Environ. Earth Sci.* **2021**, *80*, 64. [CrossRef]
2. Farah, K.; Mejri, A.; Hosni, F.; Ben Ouada, H.; Fuochi, P.G.; Lavalle, M.; Kovács, A. Characterization of a silicate glass as a high dose dosimeter. *Nucl. Instrum. Methods Phys. Res. Sect. A Accel. Spectrometers Detect. Assoc. Equip.* **2010**, *614*, 137–144. [CrossRef]
3. DWK Life Sciences Glassware Technical Information. *Glas. Types Prop.* **2022**, 12–19.
4. Jubier, N.J. Estimation of Radiation Shielding Properties for Composites Material Based Unsaturated Polyester Filled with Granite and Iron Particles. *J. Multidiscip. Eng. Sci. Stud.* **2017**, *3*, 1309–1316.
5. Khanna, A.; Bhatti, S.S.; Singh, K.J.; Thind, K.S. Gamma-ray attenuation coefficients in some heavy metal oxide borate glasses at 662 keV. *Nucl. Instrum. Methods Phys. Res. Sect. B Beam Interact. Mater. Atoms* **1996**, *114*, 217–220. [CrossRef]
6. Oto, B.; Gür, A.; Kavaz, E.; Çakır, T.; Yaltay, N. Determination of gamma and fast neutron shielding parameters of magnetite concretes. *Prog. Nucl. Energy* **2016**, *92*, 71–80. [CrossRef]
7. Mesbahi, A.; Ghiasi, H. Shielding properties of the ordinary concrete loaded with micro-and nano-particles against neutron and gamma radiations. *Appl. Radiat. Isot.* **2018**, *136*, 27–31. [CrossRef]
8. Shimizu, A.; Onda, T.; Sakamoto, Y. Calculation of gamma-ray buildup factors up to depths of 100 mfp by the method of invariant embedding, (III). *J. Nucl. Sci. Technol.* **2004**, *41*, 413–424. [CrossRef]
9. Singh, K.; Singh, H.; Sharma, V.; Nathuram, R.; Khanna, A.; Kumar, R.; Singh Bhatti, S.; Singh Sahota, H. Gamma-ray attenuation coefficients in bismuth borate glasses. *Nucl. Instrum. Methods Phys. Res. Sect. B Beam Interact. Mater. Atoms* **2002**, *194*, 1–6. [CrossRef]
10. Durani, L. Update to ANSI/ANS-6.4.3-1991 for Low-Z and Compound Materials and Review of Particle Transport Theory. Master's Thesis, University of Nevada, Las Vegas, NV, USA, 2009.
11. Dawoud, M.M.A.; Hegazi, M.M.; Saleh, H.M.; El Helew, W.K. Removal of stable and radio isotopes from wastewater by using modified microcrystalline cellulose based on Taguchi L16. *Int. J. Environ. Sci. Technol.* **2022**, 1–12. [CrossRef]
12. Dawoud, M.M.A.; Hegazy, M.M.; Helew, W.K.; Saleh, H.M. Overview of Environmental Pollution and Clean Management of Heavy Metals and Radionuclides by using Microcrystalline Cellulose. *J. Nucl. Energy Sci. Power Gener. Technol.* **2021**, *3*, 2.
13. Saleh, H.M.; Bondouk, I.I.; Salama, E.; Esawii, H.A. Consistency and shielding efficiency of cement-bitumen composite for use as gamma-radiation shielding material. *Prog. Nucl. Energy* **2021**, *137*, 103764. [CrossRef]
14. Reda, S.M.; Saleh, H.M. Calculation of the gamma radiation shielding efficiency of cement-bitumen portable container using MCNPX code. *Prog. Nucl. Energy* **2021**, *142*, 104012. [CrossRef]
15. Eid, M.S.; Bondouk, I.I.; Saleh, H.M.; Omar, K.M.; Sayyed, M.I.; El-Khatib, A.M.; Elsafi, M. Implementation of waste silicate glass into composition of ordinary cement for radiation shielding applications. *Nucl. Eng. Technol.* **2021**, *54*, 1456–1463. [CrossRef]
16. Eskander, S.B.; Saleh, H.M.; Tawfik, M.E.; Bayoumi, T.A. Towards potential applications of cement-polymer composites based on recycled polystyrene foam wastes on construction fields: Impact of exposure to water ecologies. *Case Stud. Constr. Mater.* **2021**, *15*, e00664. [CrossRef]

17. Saleh, H.; Salman, A.; Faheim, A.; El-Sayed, A. Polymer and polymer waste composites in nuclear and industrial applications. *J. Nucl. Energy Sci. Power Gener. Technol.* **2020**, *9*, 1000199.
18. Saleh, H.M.; Eskander, S.B. Impact of water flooding on hard cement-recycled polystyrene composite immobilizing radioactive sulfate waste simulate. *Constr. Build. Mater.* **2019**, *222*, 522–530. [CrossRef]
19. Saleh, H.M.; El-Saied, F.A.; Salaheldin, T.A.; Hezo, A.A. Influence of severe climatic variability on the structural, mechanical and chemical stability of cement kiln dust-slag-nanosilica composite used for radwaste solidification. *Constr. Build. Mater.* **2019**, *218*, 556–567. [CrossRef]
20. Saleh, H.M.; El-Sheikh, S.M.; Elshereafy, E.E.; Essa, A.K. Performance of cement-slag-titanate nanofibers composite immobilized radioactive waste solution through frost and flooding events. *Constr. Build. Mater.* **2019**, *223*, 221–232. [CrossRef]
21. Saleh, H.M.; Salman, A.A.; Faheim, A.A.; El-Sayed, A.M. Sustainable composite of improved lightweight concrete from cement kiln dust with grated poly (styrene). *J. Clean. Prod.* **2020**, *277*, 123491. [CrossRef]
22. Saleh, H.M.; Salman, A.A.; Faheim, A.A.; El-Sayed, A.M. Influence of aggressive environmental impacts on clean, lightweight bricks made from cement kiln dust and grated polystyrene. *Case Stud. Constr. Mater.* **2021**, *15*, e00759. [CrossRef]
23. Singh, V.P.; Badiger, N.M.; Kaewkhao, J. Radiation shielding competence of silicate and borate heavy metal oxide glasses: Comparative study. *J. Non-Cryst. Solids* **2014**, *404*, 167–173. [CrossRef]
24. Sayyed, M.I.; Tekin, H.O.; Kılıcoglu, O.; Agar, O.; Zaid, M.H.M. Shielding features of concrete types containing sepiolite mineral: Comprehensive study on experimental, XCOM and MCNPX results. *Results Phys.* **2018**, *11*, 40–45. [CrossRef]
25. Hanumantharayappa, C. Study of gamma, X-ray and neutron shielding parameters of some alloys. *IJPAP* **2018**, *56*, 631–634.
26. Abouhaswa, A.S.; Tekin, H.O.; Ahmed, E.M.; Kilicoglu, O.; Rammah, Y.S. Synthesis, physical, linear optical and nuclear radiation shielding characteristics of B_2O_3–BaO–PbO–SrO_2 glasses. *J. Mater. Sci. Mater. Electron.* **2021**, *32*, 18163–18177. [CrossRef]
27. Al-Hadeethi, Y.; Sayyed, M.I. Analysis of borosilicate glasses doped with heavy metal oxides for gamma radiation shielding application using Geant4 simulation code. *Ceram. Int.* **2019**, *45*, 24858–24864. [CrossRef]
28. Zaid, M.H.M.; Matori, K.A.; Abdul Aziz, S.H.; Zakaria, A.; Ghazali, M.S.M. Effect of ZnO on the physical properties and optical band gap of soda lime silicate glass. *Int. J. Mol. Sci.* **2012**, *13*, 7550–7558. [CrossRef]
29. Dong, M.G.; Sayyed, M.I.; Lakshminarayana, G.; Çelikbilek Ersundu, M.; Ersundu, A.E.; Nayar, P.; Mahdi, M.A. Investigation of gamma radiation shielding properties of lithium zinc bismuth borate glasses using XCOM program and MCNP5 code. *J. Non-Cryst. Solids* **2017**, *468*, 12–16. [CrossRef]
30. Tekin, H.O.; Altunsoy, E.E.; Kavaz, E.; Sayyed, M.I.; Agar, O.; Kamislioglu, M. Photon and neutron shielding performance of boron phosphate glasses for diagnostic radiology facilities. *Results Phys.* **2019**, *12*, 1457–1464. [CrossRef]
31. Sayyed, M.I.; Rammah, Y.S.; Abouhaswa, A.S.; Tekin, H.O.; Elbashir, B.O. ZnO-B_2O_3-PbO glasses: Synthesis and radiation shielding characterization. *Phys. B Condens. Matter* **2018**, *548*, 20–26. [CrossRef]
32. Hussein, K.I.; Alqahtani, M.S.; Alzahrani, K.J.; Alqahtani, F.F.; Zahran, H.Y.; Alshehri, A.M.; Yahia, I.S.; Reben, M.; Yousef, E.S. The Effect of ZnO, MgO, TiO2, and Na2O Modifiers on the Physical, Optical, and Radiation Shielding Properties of a TeTaNb Glass System. *Materials* **2022**, *15*, 1844. [CrossRef]
33. Tijani, S.A.; Kamal, S.M.; Al-Hadeethi, Y.; Arib, M.; Hussein, M.A.; Wageh, S.; Dim, L.A. Radiation shielding properties of transparent erbium zinc tellurite glass system determined at medical diagnostic energies. *J. Alloys Compd.* **2018**, *741*, 293–299. [CrossRef]
34. Shams, T.; Eftekhar, M.; Shirani, A. Investigation of gamma radiation attenuation in heavy concrete shields containing hematite and barite aggregates in multi-layered and mixed forms. *Constr. Build. Mater.* **2018**, *182*, 35–42. [CrossRef]
35. Kindrat, I.I.; Padlyak, B.V.; Drzewiecki, A. Intrinsic luminescence of un-doped borate glasses. *J. Lumin.* **2017**, *187*, 546–554. [CrossRef]
36. Singh, N.; Singh, K.J.; Singh, K.; Singh, H. Comparative study of lead borate and bismuth lead borate glass systems as gamma-radiation shielding materials. *Nucl. Instrum. Methods Phys. Res. Sect. B Beam Interact. Mater. Atoms* **2004**, *225*, 305–309. [CrossRef]
37. AlBuriahi, M.S.; Hegazy, H.H.; Alresheedi, F.; Olarinoye, I.O.; Algarni, H.; Tekin, H.O.; Saudi, H.A. Effect of CdO addition on photon, electron, and neutron attenuation properties of boro-tellurite glasses. *Ceram. Int.* **2021**, *47*, 5951–5958. [CrossRef]
38. Kaur, R.; Singh, S.; Pandey, O.P. Structural variation in gamma ray irradiated PbO-Na_2O-B_2O_3-SiO_2 glasses. *Solid State Commun.* **2014**, *188*, 40–44. [CrossRef]
39. Marzouk, S.Y.; Seoudi, R.; Said, D.A.; Mabrouk, M.S. Linear and non-linear optics and FTIR characteristics of borosilicate glasses doped with gadolinium ions. *Opt. Mater.* **2013**, *35*, 2077–2084. [CrossRef]
40. Bootjomchai, C.; Laopaiboon, J.; Yenchai, C.; Laopaiboon, R. Gamma-ray shielding and structural properties of barium-bismuth-borosilicate glasses. *Radiat. Phys. Chem.* **2012**, *81*, 785–790. [CrossRef]
41. Salama, E.; Soliman, H.A.; Youssef, G.M.; Hamad, S. Thermoluminescence Properties of Borosilicate Glass Doped with ZnO Thermoluminescence properties of borosilicate glass doped with ZnO. *J. Lumin.* **2018**, *186*, 164–169. [CrossRef]
42. Alajerami, Y.S.M.; Hashim, S.; Ghoshal, S.K.; Bradley, D.A.; Mhareb, M.; Saleh, M.A. Copper doped borate dosimeters revisited. *J. Lumin.* **2014**, *155*, 141–148. [CrossRef]
43. Mhareb, M.H.A.; Alqahtani, M.; Alshahri, F.; Alajerami, Y.S.M.; Saleh, N.; Alonizan, N.; Sayyed, M.I.; Ashiq, M.G.B.; Ghrib, T.; Al-Dhafar, S.I.; et al. The impact of barium oxide on physical, structural, optical, and shielding features of sodium zinc borate glass. *J. Non-Cryst. Solids* **2020**, *541*, 120090. [CrossRef]

44. Rammah, Y.S.; Tekin, H.O.; Sriwunkum, C.; Olarinoye, I.; Alalawi, A.; Al-Buriahi, M.S.; Nutaro, T.; Tonguc, B.T. Investigations on borate glasses within SBC-Bx system for gamma-ray shielding applications. *Nucl. Eng. Technol.* **2021**, *53*, 282–293. [CrossRef]
45. Aly, P.; El-Kheshen, A.A.; Abou-Gabal, H.; Agamy, S. Structural investigation and measurement of the shielding effect of borosilicate glass containing PbO, SrO, and BaO against gamma irradiation. *J. Phys. Chem. Solids* **2020**, *145*, 109521. [CrossRef]
46. Sayed El-Ahll, L.; Salama, E.; Saudi, H.A.; Alazab, H.A.; Ghany, H.A.A. The Effect of Barium on the Nuclear Radiation Shielding Capabilities of Nickel-Reinforced Borosilicate Glasses. *Silicon* **2022**, *14*, 8909–8917. [CrossRef]
47. Kavas, T.; Alsufyani, S.J.; Alrowaili, Z.A.; Tamam, N.; Kurtulus, R.; Olarinoye, I.O.; Al-Buriahi, M.S. Influence of iron (III) oxide on the optical, mechanical, physical, and radiation shielding properties of sodium-barium-vanadate glass system. *Optik* **2022**, *257*. [CrossRef]
48. Mhareb, M.H.A.; Alqahtani, M.; Alajerami, Y.S.M.; Alshahri, F.; Sayyed, M.I.; Mahmoud, K.A.; Saleh, N.; Alonizan, N.; Al-Buriahi, M.S.; Kaky, K.M. Ionizing radiation shielding features for titanium borosilicate glass modified with different concentrations of barium oxide. *Mater. Chem. Phys.* **2021**, *272*, 125047. [CrossRef]
49. Aboalatta, A.; Asad, J.; Humaid, M.; Musleh, H.; Shaat, S.K.K.; Ramadan, K.; Sayyed, M.I.; Alajerami, Y.; Aldahoudi, N. Experimental investigation of zinc sodium borate glass systems containing barium oxide for gamma radiation shielding applications. *Nucl. Eng. Technol.* **2021**, *53*, 3058–3067. [CrossRef]
50. Abdel-Baki, M.; Salem, A.M.; Abdel-Wahab, F.A.; El-Diasty, F. Bond character, optical properties and ionic conductivity of $Li_2O/B_2O_3/SiO_2/Al_2O_3$ glass: Effect of structural substitution of Li_2O for LiCl. *J. Non-Cryst. Solids* **2008**, *354*, 4527–4533. [CrossRef]
51. Singh, D.; Singh, K.; Singh, G.; Manupriya; Mohan, S.; Arora, M.; Sharma, G. Optical and structural properties of ZnO-PbO-B_2O_3 and ZnO-PbO-B_2O_3-SiO_2 glasses. *J. Phys. Condens. Matter* **2008**, *20*, 075228. [CrossRef]
52. Rammah, Y.S.; Sayyed, M.I.; Ali, A.A.; Tekin, H.O.; El-Mallawany, R. Optical properties and gamma-shielding features of bismuth borate glasses. *Appl. Phys. A Mater. Sci. Process.* **2018**, *124*, 832. [CrossRef]
53. Rammah, Y.S.; Sayyed, M.I.; Abohaswa, A.S.; Tekin, H.O. FTIR, electronic polarizability and shielding parameters of B_2O_3 glasses doped with SnO_2. *Appl. Phys. A Mater. Sci. Process.* **2018**, *124*, 650. [CrossRef]
54. Bashter, I.I. Calculation of radiation attenuation coefficients for shielding concretes. *Ann. Nucl. Energy* **1997**, *24*, 1389–1401. [CrossRef]
55. Thakur, S.; Thakur, V.; Kaur, A.; Singh, L. Structural, optical and thermal properties of nickel doped bismuth borate glasses. *J. Non-Cryst. Solids* **2019**, *512*, 60–71. [CrossRef]
56. Gaafar, I.; El-Shershaby, A.; Zeidan, I.; El-Ahll, L.S. Natural radioactivity and radiation hazard assessment of phosphate mining, Quseir-Safaga area, Central Eastern Desert, Egypt. *NRIAG J. Astron. Geophys.* **2016**, *5*, 160–172. [CrossRef]
57. Umar, S.A.; Halimah, M.K.; Chan, K.T.; Amirah, A.A.; Azlan, M.N.; Grema, L.U.; Hamza, A.M.; Ibrahim, G.G. Optical and structural properties of rice husk silicate incorporated borotellurite glasses doped with erbium oxide nanoparticles. *J. Mater. Sci. Mater. Electron.* **2019**, *30*, 18606–18616. [CrossRef]
58. Sayyed, M.I.; Qashou, S.I.; Khattari, Z.Y. Radiation shielding competence of newly developed TeO_2-WO_3 glasses. *J. Alloys Compd.* **2017**, *696*, 632–638. [CrossRef]
59. Sathiyaraj, P.; Samuel, E.J.J.; Valeriano, C.C.S.; Kurudirek, M. Effective atomic number and buildup factor calculations for metal nano particle doped polymer gel. *Vacuum* **2017**, *143*, 138–149. [CrossRef]
60. Kavaz, E.; Yorgun, N.Y. Gamma ray buildup factors of lithium borate glasses doped with minerals. *J. Alloys Compd.* **2018**, *752*, 61–67. [CrossRef]
61. El-Kameesy, S.U.; Youssef, G.M.; El-Zaiat, S.Y.; Saudi, H.A.; Abd El-Kawy, F.S. Gamma Rays Attenuation Properties and the Associated Optical and Mechanical Behavior of Development (70-x) B_2O_3-10Al_2O_3-10Na_2O-10ZnO-x PbO Glasses. *Silicon* **2018**, *10*, 1881–1886. [CrossRef]
62. Harima, Y. An historical review and current status of buildup factor calculations and applications. *Radiat. Phys. Chem.* **1993**, *41*, 631–672. [CrossRef]
63. Kaplan, M.F. *Concrete Radiation Shielding: Nuclear Physics, Concrete Properties, Design and Construction*; Longman Scientific & Technical: New York, NY, USA, 1989; ISBN 0470213388.
64. Singh, V.P.; Badiger, N.M. Gamma ray and neutron shielding properties of some alloy materials. *Ann. Nucl. Energy* **2014**, *64*, 301–310. [CrossRef]
65. *ANSI/ANS-6.4.3*; Gamma-Ray Attenuation Coefficients and Buildup Factors for Engineering Materials. American Nuclear Society: La Grange Park, IL, USA, 1991.
66. Gomaa, H.M.; Yahia, I.S.; Zahren, H.Y.; Saudi, H.A.; El-Dosokey, A.H. Effect of replacement of SiO_2 with $BaTiO_3$ on the cadmium calcium-borate glass: Aiming to obtain an active glass for optical and shielding applications. *Radiat. Phys. Chem.* **2022**, *193*, 109955. [CrossRef]
67. Huang, W.J.; Wen, Z.X.; Li, L.J.; Ashraf, G.A.; Chen, L.P.; Lei, L.; Guo, H.; Li, X.M. Photoluminescence and X-ray excited scintillating properties of Tb3+-doped borosilicate aluminate glass scintillators. *Ceram. Int.* **2022**, *48*, 17178–17184. [CrossRef]
68. Shajan, D.; Murugasen, P.; Sagadevan, S. Analysis on the structural, spectroscopic, and dielectric properties of borate glass. *Dig. J. Nanomater. Biostruct.* **2016**, *11*, 177–183.
69. Mustafa, I.S.; Kamari, H.M.; Wan Yusoff, W.M.D.; Aziz, S.A.; Rahman, A.A. Structural and optical properties of lead-boro-tellurite glasses induced by Gamma-ray. *Int. J. Mol. Sci.* **2013**, *14*, 3201–3214. [CrossRef]

70. Yadav, A.K.; Gautam, C.R. Structural and optical studies of Fe2O3 doped barium strontium titanate borosilicate glasses. *Indian J. Pure Appl. Phys.* **2015**, *53*, 42–48.
71. Rani, S.; Sanghi, S.; Agarwal, A.; Seth, V.P. Study of optical band gap and FTIR spectroscopy of $Li_2O{\cdot}Bi_2O_3{\cdot}P_2O_5$ glasses. *Spectrochim. Acta—Part A Mol. Biomol. Spectrosc.* **2009**, *74*, 673–677. [CrossRef]
72. Yadav, A.K.; Gautam, C.R. Synthesis, structural and optical studies of barium strontium titanate borosilicate glasses doped with ferric oxide. *Spectrosc. Lett.* **2015**, *48*, 514–520. [CrossRef]
73. Gautam, C.; Yadav, A.K.; Mishra, V.K.; Vikram, K. Synthesis, IR and Raman Spectroscopic Studies of (Ba,Sr)TiO_3 Borosilicate Glasses with Addition of La_2O_3. *Open J. Inorg. Non-Metallic Mater.* **2012**, *2*, 47–54. [CrossRef]
74. Gautam, C.R.; Kumar, D.; Parkash, O. IR study of Pb-Sr titanate borosilicate glasses. *Bull. Mater. Sci.* **2010**, *33*, 145–148. [CrossRef]
75. Mandal, A.K.; Agrawal, D.; Sen, R. Preparation of homogeneous barium borosilicate glass using microwave energy. *J. Non-Cryst. Solids* **2013**, *371–372*, 41–46. [CrossRef]
76. Study, S.; Consumption, L.E.; Part, D.U.; Utilization, D.; Yoshizawa, N.; Harimoto, K.; Ichihara, M.; Miki, Y.; Takase, K.; Inoue, T. Synthesis, Characterization and Bioactive Study of Borosilicate Sol-Gel Glass Khairy. *Nat. Sci.* **2015**, *13*, 475–476.
77. Rada, S.; Dehelean, A.; Culea, E. FTIR and UV-VIS spectroscopy investigations on the structure of the europium-lead-tellurate glasses. *J. Non-Cryst. Solids* **2011**, *357*, 3070–3073. [CrossRef]
78. Saudi, H.A.; Abd-Allah, W.M.; Shaaban, K.S. Investigation of gamma and neutron shielding parameters for borosilicate glasses doped europium oxide for the immobilization of radioactive waste. *J. Mater. Sci. Mater. Electron.* **2020**, *31*, 6963–6976. [CrossRef]
79. Alzahrani, J.S.; Alrowaili, Z.A.; Olarinoye, I.O.; Alothman, M.A.; Al-Baradi, A.M.; Kebaili, I.; Al-Buriahi, M.S. Nuclear shielding properties and buildup factors of Cr-based ferroalloys. *Prog. Nucl. Energy* **2021**, *141*, 103956. [CrossRef]